Acta Materialia 234 (2022) 117987

Contents lists available at ScienceDirect

Acta Materialia

journal homepage: www.elsevier.com/locate/actamat

Full length article

Strain-tuning of transport gaps and semiconductor-to-conductor phase transition in twinned graphene

F. Arca[a], J.P. Mendez[b], M. Ortiz[c], M.P. Ariza[a,*]

[a] Escuela Técnica Superior de Ingeniería, Universidad de Sevilla, Camino de los descubrimientos, s.n., 41092 Sevilla, Spain
[b] Sandia National Laboratories, Albuquerque, 87123, NM, USA
[c] Division of Engineering and Applied Science, California Institute of Technology, CA 91125 Pasadena, USA

ARTICLE INFO

Article history:
Received 24 February 2022
Revised 20 April 2022
Accepted 28 April 2022
Available online 7 May 2022

Keywords:
Graphene
Geometrical twinning
Phase transformation
Critical phenomena

ABSTRACT

We show, through the use of the Landauer-Büttiker (LB) formalism and a tight-binding (TB) model, that the transport gap of twinned graphene can be tuned through the application of a uniaxial strain in the direction normal to the twin band. Remarkably, we find that the transport gap E_{gap} bears a square-root dependence on the control parameter $\epsilon_x - \epsilon_c$, where ϵ_x is the applied uniaxial strain and $\epsilon_c \sim 19\%$ is a critical strain. We interpret this dependence as evidence of criticality underlying a continuous phase transition, with $\epsilon_x - \epsilon_c$ playing the role of control parameter and the transport gap E_{gap} playing the role of order parameter. For $\epsilon_x < \epsilon_c$, the transport gap is non-zero and the material is semiconductor, whereas for $\epsilon_x > \epsilon_c$ the transport gap closes to zero and the material becomes conductor, which evinces a semiconductor-to-conductor phase transition. The computed critical exponent of 1/2 places the transition in the meanfield universality class, which enables far-reaching analogies with other systems in the same class.

1. Introduction

Graphene has been widely investigated as a basis for post-silicon generation nanoelectronics, owing to its outstanding mechanical [1] and electronic properties [2]. Material engineering techniques such as coupling graphene layers to a hexagonal boron nitride substrate [3,4], introducing doping elements [5], or cutting graphene layers into narrow nanoribbons [6], can induce from small to medium transport gaps (0.1–0.6 eV) required for nanoelectronic applications. In addition, techniques that combine different graphene domains with varying electronic structures can open higher transport gaps [7]. For instance, asymmetric grain boundaries and twin structures can induce transport gaps as large as 1.54 eV [8] and 1.15 eV [9], respectively.

Electronic component manufacturing may require other material properties, depending on the application. Piezoelectricity, the best-known form of electromechanical coupling, is commonly observed in non-centrosymmetric crystals, and graphene does not naturally exhibit this property. However, breaking the symmetry at surfaces and interfaces within the graphene lattice can cause other forms of electromechanical coupling to appear, i.e., surface piezoelectricity and flexoelectricity [10]. This idea has theoretically allowed enabling electromechanical properties in graphene through various techniques, such as functionalization and doping [11,12], induced curvature [13,14], and by introducing triangular pores in graphene layers [10] and nanoribbons [15]. Specifically, a triangular pore causes a non-uniform strain gradient across a graphene layer under uniaxial strain, which modifies the ionic positions and leads to an asymmetric redistribution of the electron density, which induces a variation in flexoelectric polarization [16].

Symmetry-breaking configurations under strain can also result in transport gaps that are tunable in graphene sheets [17,18], nanoribbons [19], and grain boundaries [20,21], since the application of strain modifies the local band structure of the graphene lattice [22]. Controlling electronic properties by strain would enable the use of graphene to fabricate flexible and sensitive pressure sensors [23], transformers, transducers and energy harvesters [24–26], and other applications. In these applications, the ability of graphene to sustain large strains up to 25% is of the essence [1].

Twins are known low-energy structures in graphene [27,28] that combine lattice variants, or phases, in contiguous regions separated by interfaces, or twin boundaries. The variants are generated by lattice-preserving shears and rotations that are

* Corresponding author.
E-mail address: mpariza@us.es (M.P. Ariza).

https://doi.org/10.1016/j.actamat.2022.117987

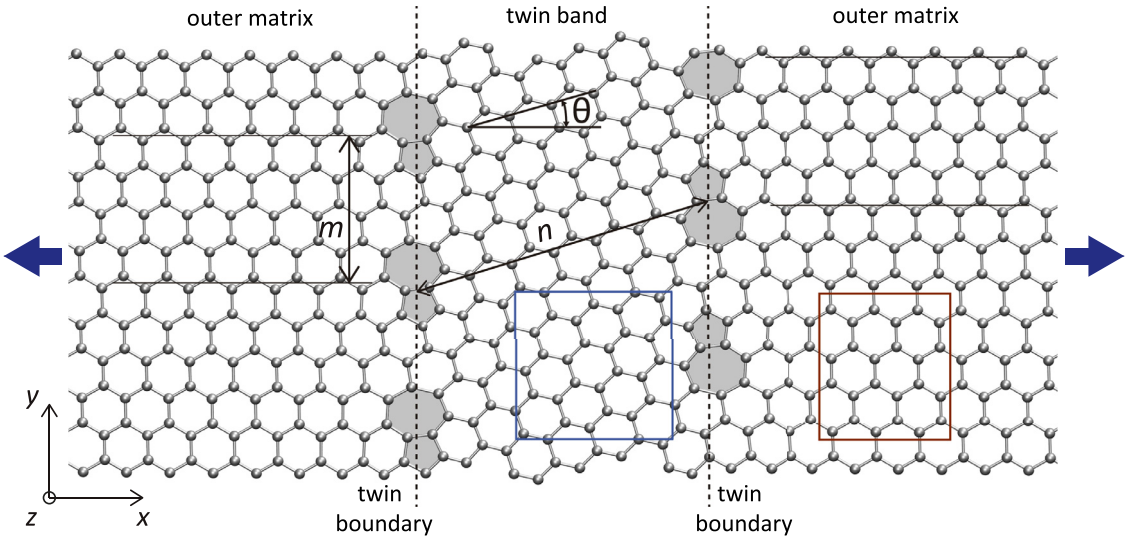

Fig. 1. Fully-relaxed atomic configuration of the (15,8) twin. Also shown are the twin band and outer matrix regions abutting on the twin boundary and the computational sub-cells (blue and red) used for the band structure analysis. (For interpretation of the references to colour in this figure legend, the reader is referred to the web version of this article.)

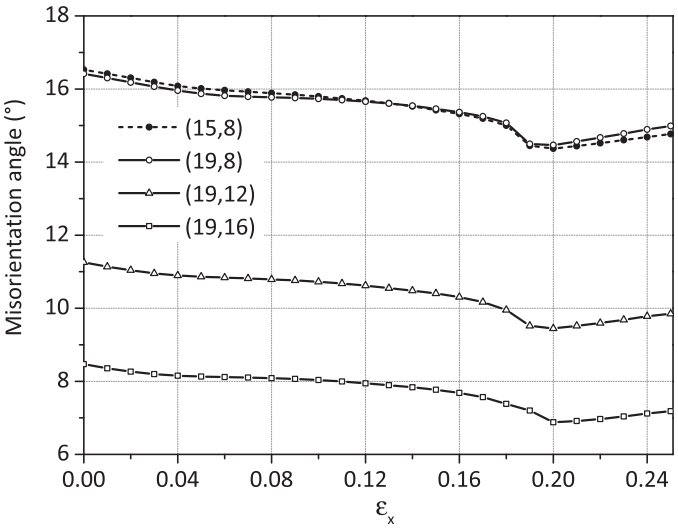

Fig. 2. Variation of the misorientation angle with applied uniaxial strain in (15,8), (19,8), (19,12) and (19,16) twins.

coherent across the interfaces and satisfy several specific twinning relations [29]. Graphene twins have been computationally studied by introducing twinning boundaries in the crystal *ab initio* [30,31]. Alternatively, twinned configurations can be generated by introducing, and subsequently relaxing, arrays of dislocations in the graphene lattice [32], proving that twinning works as an accommodation mechanism in graphene and that it results in stable low-energy configurations. These studies have shown that graphene twins can induce transport gaps of comparable magnitude to those induced by grain boundaries.

In this work, we investigate the effects of uniaxial strain on the electronic properties of twin structures in graphene. We start by computing the equilibrium configurations employing the molecular dynamics software LAMMPS [33] and using the AIREBO interatomic potential [34], and subsequently we evaluate their charge-carrier transmission properties by means of the Landauer-Büttiker (LB) formalism [35–37] in combination with a tight-binding (TB) model [38]. By way of verification, we additionally calculate selected band structures of the strained twins using the DFT code VASP [39,40]. Finally, we calculate the evolution of the polarization under strain using the DFT code SIESTA [41]. These computational methods have been extensively tested and used in previous publications [9,32,42,43].

2. Methods

2.1. Generation of twinning configurations

Following the methodology described in [32], we compute the twinning configurations in two steps. In the first step, we use a harmonic lattice model [43], with force constants derived from the second version of the Long-Range Carbon-Order Potential (LCBOPII) [44], in order to insert periodic discrete dislocations dipoles in a pristine graphene lattice. Specifically, the dislocation dipoles are inserted through lattice-invariant slips [45,46]. In the second step, the initial harmonic configurations obtained in the first step are fully relaxed using the LAMMPS code [33] together with the AIREBO potential [34]. The simulations combine canonical ensemble molecular dynamics (NVT MD) at low temperature ($T = 1.0$ K) with a subsequent conjugate-gradient (CG) energy minimization aimed at obtaining fully-relaxed configurations.

We also use the LAMMPS software and the AIREBO interatomic potential to apply a uniform uniaxial strain. The twinning configurations are progressively deformed up to a final total strain of $\epsilon_{x_{\max}} = 0.25$, by the application of successive strain increments of $\epsilon_{x_{step}} = 0.01$. Each step entails three different calculations: a) uniform stretching of the length of the computational cell along the x-axis to length $L_x = L_0(1 + \epsilon_x)$, where L_0 is the length of the undeformed computational cell; b) CG relaxation in the y-dimension of the cell, so as to account for the Poisson effect; c) NVT MD at low temperature. Steps (b) and (c) are repeated as needed to ensure that the deformed twinning structures are in equilibrium. Out-of-plane displacements are constrained and periodic boundary conditions are applied throughout all calculations.

2.2. Transport gap calculations

To evaluate the transport gap across the twinning configurations we follow the methodology set forth in [9,42], which is based on the Landauer-Büttiker (LB) formalism [35–37] in combination with a transferable tight-binding (TB) model for carbon [38]. The

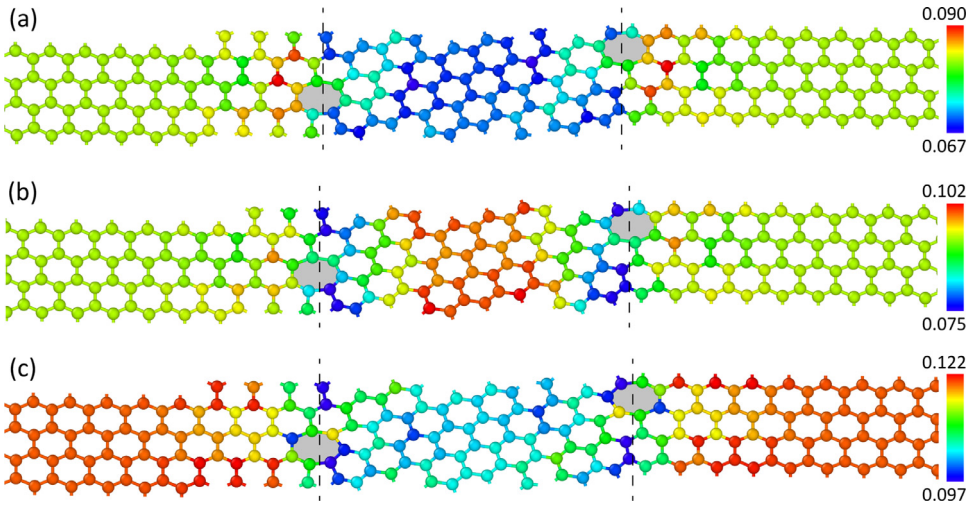

Fig. 3. Local areal strain $\sim \epsilon_x + \epsilon_y$ distribution for the (15,8) twin at a) $\epsilon_x = 0.17$; b) $\epsilon_x = 0.19$; and c) $\epsilon_x = 0.23$.

LB formalism provides a framework for the calculation of coherent electronic transport across a device, which is comprised of three parts. The central part consists of the twinned structures whose transmission properties are to be evaluated. At both ends of this central part, two regions of pristine graphene are attached that are semi-infinite in the x-direction. Further details of this framework can be found in Supplementary Material 2.

For each configuration, we calculate the transmission coefficient with respect to electronic energy. From this curve, we obtain the transport gap of that configuration as the energy range in which the transmission is ostensibly zero. All calculations are carried out over a grid of 144 k-points (with $\eta = 0.01$), which affords converged results. We have used the tight-binding parameters for carbon reported in [38].

2.3. Band structure calculations

The VASP [39,40] code, which employs a plane wave basis set, is used for the DFT calculations of the band structures. Specifically, a projector augmented wave potential with the PBE exchange-correlation functional is used. The partial occupancies are set by recourse to a Gaussian smearing of 0.05eV. The charge density is computed over a 30×30 Gamma centered grid. In calculations, we use a range of methods of varying fidelities, with the lower-fidelity models applied to the larger computational cells and the high-fidelity models used mainly for validation over small subsystems.

2.4. Polarization calculations

The polarization calculations are carried out using the DFT software SIESTA [41], which computes the total polarization as the sum of the ionic contribution, defined as the sum of the atomic positions within the unit cell multiplied by their ionic charges, and the electronic contribution, which is calculated as a Berry phase of the electronic Bloch wavefunctions [47]. The Berry phase approach can only be applied at zero temperature and electric field.

These calculations employed the PBE exchangecorrelation functional within the generalized gradient approximation (GGA) [48], the double-ξ plus polarization basis set [49], smooth norm-conserving pseudopotentials [50], a grid of 80 k-points in the reciprocal space, and a mesh cutoff of 400 Ry.

Due to the multi-valuedness of the polarization, we chose the values in the interval $\{-P_{q,i}, P_{q,i}\}$, where $P_{q,i} = \frac{1}{A} e R_i$ is the polarization quantum along the i-direction, with A the area of the computational cell, e the elementary charge and R_i the length of the ith lattice vector.

3. Results and discussion

We consider twinned microstructures such as described in [32], which are the result of inserting periodic arrays of parallel dislocation dipoles into single graphene layers (see Section 2.1). As an example, in Fig. 1 we show the dislocation structures attendant to a (15,8) twin, in the nomenclature of [32]. The twinned microstructure consists of three nearly-perfect lattices, separated by linear arrays of 7-5 ring defects. The region between the dislocation-dipole array, or twin band, is rotated by an angle of 16.5° with respect to the outer regions, or matrix. This rotation takes place spontaneously as a result of energy minimization following the introduction of the dislocation dipoles. The misorientation angle and the lattice-preserving shear strain of the twin band satisfy the classical twinning relations that identify the microstructure as a true twin [29,32].

Twinning structures in graphene can be defined by means of a pair (n, m), where n is the number of zig-zag bonds undergoing slip in a dipole, a measure of the twinned region width, and m is the number of armchair bonds between dipoles, a measure of dipole separation, cf. Fig. 1. In the present work, we focus on twinning structures with $n = 15$, since they have asymptotically stable misorientation angles and energies [32], and, in particular, on the (15,8) configuration, which has the highest transport gap among this type of twins [9]. The attendant atomic configurations are visualized in Supplementary Material 1. In addition, we apply a uniform uniaxial strain ϵ_x to these configurations along the x-axis normal to the twin band using molecular dynamics and the AIREBO [34] potential implemented in LAMMPS [33] and the methodology summarized in Section 2.1. The strain is applied progressively up to a maximum of 0.25, or $\sim 25\%$, the experimental failure strain of graphene [1].

Figure 2 shows the variation of misorientation angle with applied uniaxial strain. As may be observed, the misorientation angle decreases smoothly down to a minimum value at approximately $\epsilon_x = 0.19$, beyond which strain the angle increases slightly. The evolution of the areal strain $\sim \epsilon_x + \epsilon_y$ is shown in Fig. 3 using the OVITO software [51]. For applied strains $\epsilon_x < 0.19$, the twin band exhibits the lowest areal strain and the outside matrix is comparatively more deformed, cf. Fig. 3a. In addition, the cores of the interfacial dislocations appear as points of strain singularity. This strain ordering flips at an applied strain $\epsilon_x = 0.19$, Fig. 3b, and again for

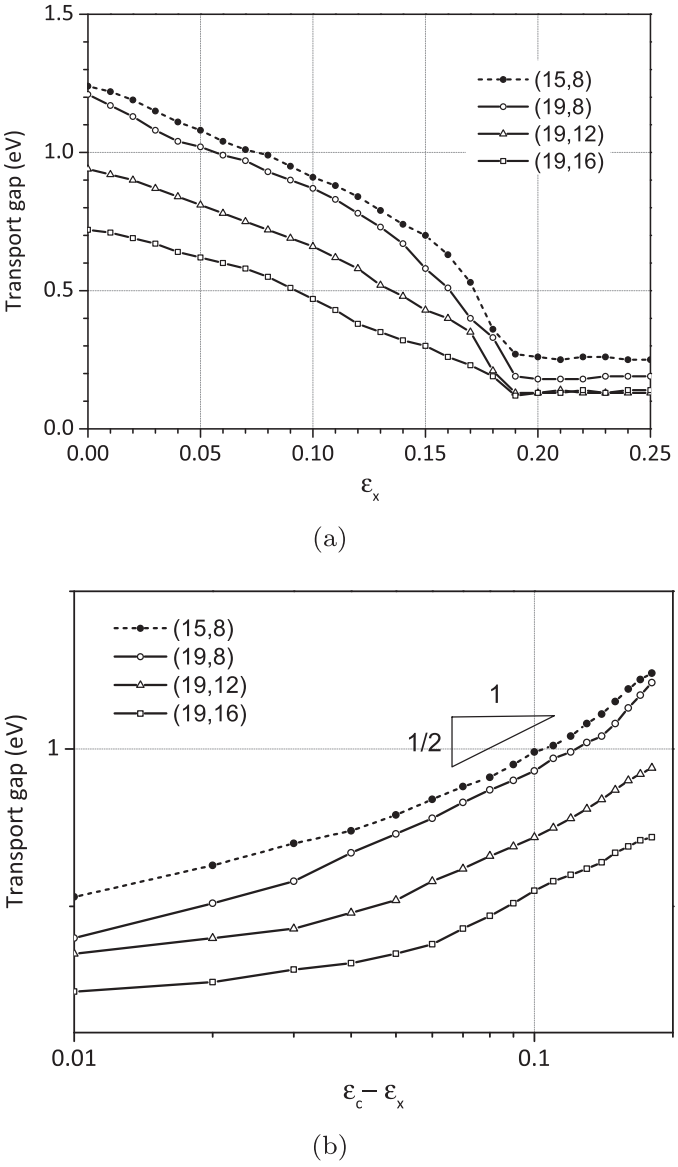

Fig. 4. a) Dependence of the transport gap on the uniaxial strain for the dislocation structures (15,8), (19,8), (19,12), (19,16). b) Log-log plot showing the critical exponent of 1/2.

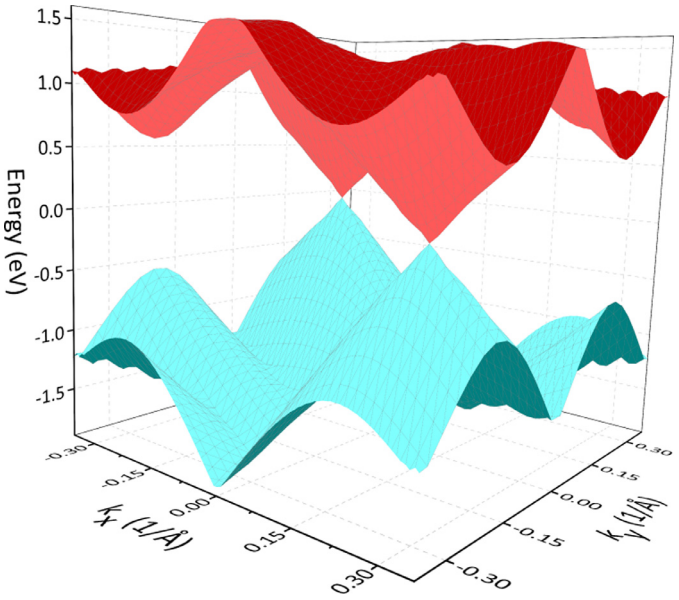

Fig. 5. Electronic band structure of a representative sub-lattice of the (15,8) twin band at zero applied strain subject to periodic boundary conditions. Valence (below) and conduction (above) bands are plotted on the first Brillouin zone.

applied strains $\epsilon_x > 0.2$, Fig. 3c, which is indicative of exchange of stability and conformational transitions occurring in the twin structure at critical applied strains along the deformation path.

Next, we turn attention to the electronic transport gap of the twinned structure and its dependence on the applied strain. As already mentioned, we calculate transport gaps by recourse to the Landauer-Büttiker (LB) formalism [35–37] in combination with a tight-binding (TB) model [38], as also employed in previous work [9,32,42,43]. This approach is computationally more efficient than DFT at comparable accuracy [9,42]. Specifically, we evaluate electronic transmission in the direction perpendicular to the twin boundaries, which is also the straining direction. Details of the computational methodology were collected in Section 2.2.

The variation of the transport gap with applied uniaxial strain is shown in Fig. 4(a) for the (15,8), (19,8), (19,12) and (19,16) twins. As previously noted [9], the transport gap decreases with increasing dislocation spacing m. In addition, we find that the application of strain causes the transport gap to decrease to nearly zero at a critical applied strain of $\epsilon_c = 0.19$, with the gap remaining ostensibly constant at larger strains. Remarkably, the dependence of the transport gap with the control parameter $\epsilon_x - \epsilon_c$ is well-approximated by a power-law of exponent 1/2 (Fig. 4(b)), in a manner strongly reminiscent of critical phenomena. We return to this possible connection in Section 4.

We additionally evaluate the band structure using VASP code, as described in Section 2.3. For the (15,8) configuration, we separately calculate the momentum-energy relation of charge carriers for the twin band and for the exterior matrix, since, by the nature of twinning, the lattice is nearly perfect in those regions and periodic boundary conditions can be applied to sub-lattices representative of those regions, cf. Fig. 1. The valence and conduction bands of the representative twinned region at zero applied strain are shown in Fig. 5 by way of example. As expected, similarly to pristine graphene the Dirac cones are connected and no transport gap opens up.

Across the twin boundaries and for elastic transmission, both energy E and momentum k_y parallel to the interface must be continuous across the interface [8]. For the (15,8) twin at zero applied strain, Fig. 6a shows a k_y-sections through the minima of the twinned and matrix regions band structures. As can be seen from the figure, the Dirac cones are significantly shifted from each other, resulting in a computed transport gap of value $E_{\text{gap}} = 1.11$ eV for the entire system. We recall that, near the Fermi level, the charge carriers in graphene satisfy the relation $E(\mathbf{k}) = \hbar v_F |\mathbf{k}|$, where $v_F = 10^6$ m/s is the Fermi velocity. Therefore, the transport gap can be approximated as $E_{\text{gap}} = \hbar v_F |k_t - k_o|$ [20], where k_t and k_o are the y-momenta of the Dirac points of the twinned and outer matrix regions, respectively. For the unstrained (15,8) twin, this relation gives $E_{\text{gap}} = 1.31$eV, which is slightly higher than, but a good approximation to, the exact value $E_{\text{gap}} = 1.11$ eV computed directly for the entire system.

As already noted, under straining the twin band and outer matrix undergo divergent deformation paths punctuated by conformational transitions at well-defined applied strains. This complex deformation redistribution in turn results in changes in the band structure. Figure 6b shows k_y-sections through the minima of the twin band and outer matrix band structures for the (15,8)-twin at applied strain 0.18. This strain causes the Dirac point k_t to ap-

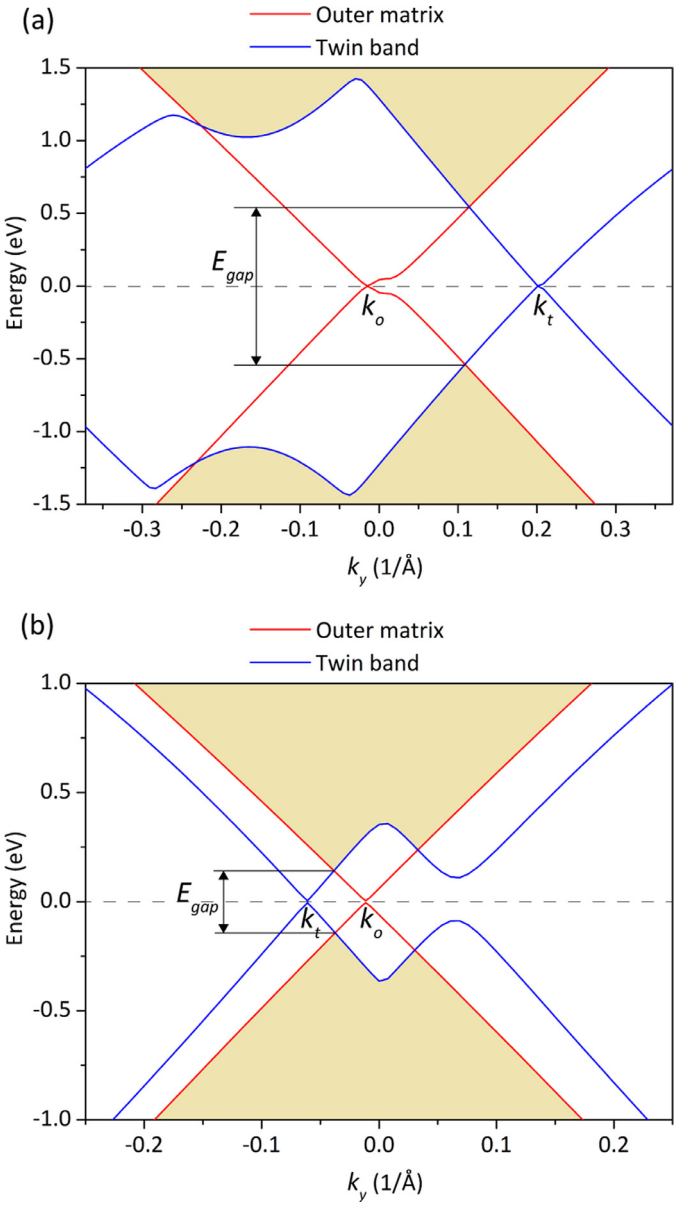

Fig. 6. k_y-sections through the minimum values of the electronic band structures of the twin band (blue) and outer matrix (red) regions of the (15,8) twin at a) $\epsilon_x = 0$, with $k_x = -0.24$ for the twin band and $k_x = 0$ for the outer matrix, and b) $\epsilon_x = 0.18$, with $k_x = -0.32$ for the twin band and $k_x = -0.15$ for the outer matrix. (For interpretation of the references to colour in this figure legend, the reader is referred to the web version of this article.)

proach k_o, which remains practically invariant, in turn causing the transport gap to decrease to the value $E_{\text{gap}} = 0.29$ eV, in keeping with the LT/TB calculations reported above.

Finally, we investigate whether strained twinned graphene exhibits piezoelectricity, a fundamental property pertaining to how systems respond to an applied electric field. Following [52], we perform polarization calculations using the DFT software SIESTA, with the setup described in Section 2.4. We note that the dipole moments in the *y*- and *z*-axis are perfectly balanced and, therefore, the polarization vector has only a *x*-component.

Figure 7 displays the dependence of the polarization on the applied uniaxial strain for the (15,8)-twin. Firstly, we observe that the twinned lattice exhibits a spontaneous polarization/cell area of 0.1895×10^{-10} C/m at zero applied strain. This spontaneous polarization results from the breaking of centrosymmetry induced by

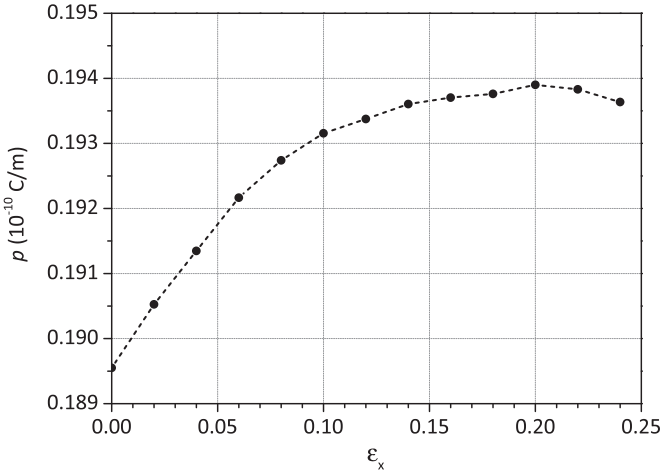

Fig. 7. Dependence of the electric polarization on the applied strain for the (15,8)-twin.

twinning and the attendant charge redistribution over the lattice. The polarization/cell area slightly increases with increasing applied strain, ostensibly saturating at 0.1950×10^{-10} C/m at the critical applied strain $\epsilon_c = 0.19$. We recall that ϵ_c is the strain at which the misorientation angle and transport gap attain their minimum values.

4. Conclusions

In conclusion, we remark that the transport gap of twinned graphene can be tuned through the application of a uniaxial strain in the direction normal to the twin band. MD calculations show that the variation of transport gap is caused by conformational changes and transitions induced by the applied strain. Such conformational changes are evinced by the variation of the misorientation of the twin band and the strain field in the twin band and the outer matrix. These conformational changes also induce a modest variation in polarization with applied strain. A relationship between transport gap and polarization has been observed in 2D materials [53]. However, it would appear that this relationship is not cause-and-effect but results from correlated variations in polarization and transport gap jointly induced by the atomic reconfigurations.

Perhaps the most remarkable feature of the tunability of twinned graphene is the evidence of critical behavior at the critical applied strain $\epsilon_c = 0.19$. This critical behavior is evident in the square-root dependence of the transport gap on $\epsilon_x - \epsilon_c$, Fig. 4. This dependence is strongly reminiscent of a continuous phase transition, with $\epsilon_x - \epsilon_c$ playing the role of control parameter and the transport gap E_{gap} playing the role of order parameter. Specifically, for $\epsilon_x < \epsilon_c$, the transport gap is non-zero and the material is semiconductor, whereas for $\epsilon_x > \epsilon_c$ the transport gap closes and the material becomes conductor. The square-root dependence of the transport gap on $\epsilon_x - \epsilon_c$ may thus be interpreted as evidence of criticality underlying a semiconductor-to-conductor phase transition. The dependence of the polarization on the control parameter $\epsilon_x - \epsilon_c$ also shows signs of critical behavior that is well-approximated by an exponent $\delta = 3$, Fig. 7. We recall that the critical exponents $\beta = 1/2$ and $\delta = 3$ are predicted by Landau, or meanfield, theory, assuming a critical dimension of 2. This interpretation in turn places strained twinned graphene in the meanfield universality class and enables far-reaching analogies with other systems in the same class, especially systems where elastic distortion mediates the interaction between local states [54].

Declaration of Competing Interest

The authors declare that they have no known competing financial interests or personal relationships that could have appeared to influence the work reported in this paper.

Acknowledgements

The authors acknowledge financial support by the Consejería de Transformación Económica, Industria, Conocimiento y Universidades of Junta de Andalucía, Spain under grant number P18-RT-1485 and the Ministerio de Ciencia, Innovación y Universidades of Spain under grant number RTI2018-094325-B-I00.

Supplementary material

Supplementary material associated with this article can be found, in the online version, at doi:10.1016/j.actamat.2022.117987.

References

[1] C. Lee, X. Wei, J.W. Kysar, J. Hone, Measurement of the elastic properties and intrinsic strength of monolayer graphene, Science 321 (5887) (2008) 385–388.
[2] A.K. Geim, K.S. Novoselov, The rise of graphene, Nat. Mater. 6 (3) (2007) 183–191.
[3] N. Kharche, S.K. Nayak, Quasiparticle band gap engineering of graphene and graphone on hexagonal boron nitride substrate, Nano Lett. 11 (12) (2011) 5274–5278.
[4] B. Hunt, J.D. Sanchez-Yamagishi, A.F. Young, M. Yankowitz, B.J. LeRoy, K. Watanabe, T. Taniguchi, P. Moon, M. Koshino, P. Jarillo-Herrero, R.C. Ashoori, Massive dirac fermions and hofstadter butterfly in a van der Waals heterostructure, Science 340 (6139) (2013) 1427–1430.
[5] P.A. Denis, Band gap opening of monolayer and bilayer graphene doped with aluminium, silicon, phosphorus, and sulfur, Chem. Phys. Lett. 492 (46) (2010) 251–257.
[6] M.Y. Han, B. Özyilmaz, Y. Zhang, P. Kim, Energy band-gap engineering of graphene nanoribbons, Phys. Rev. Lett. 98 (2007) 206805.
[7] M.C. Nguyen, V.H. Nguyen, H.-V. Nguyen, P. Dollfus, Conduction gap in graphene strain junctions: direction dependence, Semicond. Sci. Technol. 29 (11) (2014) 115024.
[8] O.V. Yazyev, S.G. Louie, Electronic transport in polycrystalline graphene, Nat. Mater. 9 (2010) 806–809.
[9] F. Arca, J.P. Mendez, M. Ortiz, M.P. Ariza, Charge-carrier transmission across twins in graphene, J. Phys. 32 (42) (2020) 425003.
[10] S.I. Kundalwal, S.A. Meguid, G.J. Weng, Strain gradient polarization in graphene, Carbon 117 (2017) 462–472.
[11] M.T. Ong, E.J. Reed, Engineered piezoelectricity in graphene, ACS Nano 6 (2) (2012) 1387–1394.
[12] K.E. El-Kelany, P. Carbonnire, A. Erba, J.-M. Sotiropoulos, M. Rrat, Piezoelectricity of functionalized graphene: aquantum-mechanical rationalization, J. Phys. Chem. C 120 (14) (2016) 7795–7803.
[13] T. Dumitric, C.M. Landis, B.I. Yakobson, Curvature-induced polarization in carbon nanoshells, Chem. Phys. Lett. 360 (1) (2002) 182–188.
[14] S. Kalinin, V. Meunier, Electronic flexoelectricity in low-dimensional systems, Phys. Rev. B 77 (2008) 033403.
[15] S. Chandratre, P. Sharma, Coaxing graphene to be piezoelectric, Appl. Phys. Lett. 100 (2) (2012) 023114.
[16] B. Javvaji, B. He, X. Zhuang, The generation of piezoelectricity and flexoelectricity in graphene by breaking the materials symmetries, Nanotechnology 29 (22) (2018) 225702.
[17] Z.H. Ni, T. Yu, Y.H. Lu, Y.Y. Wang, Y.P. Feng, Z.X. Shen, Uniaxial strain on graphene: Raman spectroscopy study and band-gap opening, ACS Nano 2 (11) (2008) 2301–2305, doi:10.1021/nn800459e.
[18] G. Gui, J. Li, J. Zhong, Band structure engineering of graphene by strain: first-principles calculations, Phys. Rev. B 78 (2008) 075435, doi:10.1103/PhysRevB.78.075435.
[19] L. Sun, Q. Li, H. Ren, H. Su, Q. Shi, J. Yang, Strain effect on electronic structures of graphene nanoribbons: a first-principles study, J. Chem. Phys. 129 (2008) 074704, doi:10.1063/1.2958285.
[20] S.B. Kumar, J. Guo, Strain-induced conductance modulation in graphene grain boundary, Nano Lett. 12 (3) (2012) 1362–1366.
[21] V. Nguyen, T. Hoang, P. Dollfus, J.-C. Charlier, Transport properties through graphene grain boundaries: strain effects: versus lattice symmetry, Nanoscale 8 (2016).
[22] M. Huang, H. Yan, T.F. Heinz, J. Hone, Probing strain-induced electronic structure change in graphene by raman spectroscopy, Nano Lett. 10 (10) (2010) 4074–4079.
[23] T.T. Tung, C. Robert, M. Castro, J.F. Feller, T.Y. Kim, K.S. Suh, Enhancing the sensitivity of graphene/polyurethane nanocomposite flexible piezo-resistive pressure sensors with magnetite nano-spacers, Carbon 108 (2016) 450–460.
[24] R. Cali, U.B. Rongala, D. Camboni, M. Milazzo, C. Stefanini, G. De Petris, C.M. Oddo, Piezoelectric energy harvesting solutions, Sensors 14 (3) (2014) 4755–4790.
[25] J. Yan, Y.G. Jeong, High performance flexible piezoelectric nanogenerators based on BaTiO3 nanofibers in different alignment modes, ACS Appl. Mater. Interfaces 8 (24) (2016) 15700–15709.
[26] S.S. Nanthakumar, X. Zhuang, H.S. Park, T. Rabczuk, Topology optimization of flexoelectric structures, J. Mech. Phys. Solids 105 (2017) 217–234.
[27] J. An, E. Voelkl, J.W. Suk, X. Li, C.W. Magnuson, L. Fu, P. Tiemeijer, M. Bischoff, B. Freitag, E. Popova, R.S. Ruoff, Domain (grain) boundaries and evidence of twinlike structures in chemically vapor deposited grown graphene, ACS Nano 5 (4) (2011) 2433–2439, doi:10.1021/nn103102a.
[28] A.P. Rooney, Z. Li, W. Zhao, A. Gholinia, A. Kozikov, G. Auton, F. Ding, R.V. Gorbachev, R.J. Young, S.J. Haigh, Anomalous twin boundaries in two dimensional materials, Nat. Commun. 9 (2018).
[29] K. Bhattacharya, Microstructure of Martensite: Why It Forms and How It Gives Rise to the Shape-Memory Effect, OUP Oxford, 2003.
[30] H. Terrones, A.L. Mackay, The geometry of hypothetical curved graphite structures, Carbon 30 (8) (1992) 1251–1260.
[31] D.F. Rojas, D. Sun, M. Ponga, Twinning in two-dimensional materials and its application to electronic properties, Electron. Struct. 1 (2) (2019) 025001.
[32] F. Arca, J.P. Mendez, M. Ortiz, M.P. Ariza, Spontaneous twinning as an accommodation mechanism in monolayer graphene, Eur. J. Mech. A. Solids 80 (2020) 103923.
[33] S. Plimpton, Fast parallel algorithms for short-range molecular dynamics, J. Comput. Phys. 117 (1) (1995) 1–19.
[34] S.J. Stuart, A.B. Tutein, J.A. Harrison, A reactive potential for hydrocarbons with intermolecular interactions, J. Chem. Phys. 112 (14) (2000) 6472–6486.
[35] S. Datta, Electronic Transport in Mesoscopic Systems, Cambridge University Press, Cambridge, 1995.
[36] S. Datta, Quantum transport: Atom to Transistor, Cambridge University Press, Cambridge, 2005.
[37] L.E.F. Foa Torres, S. Roche, J.C. Charlier, Introduction to Graphene-Based Nanomaterials: From Electronic Structure to Quantum Transport, Cambridge University Press, Cambridge, 2014.
[38] C.H. Xu, C.Z. Wang, C.T. Chan, K.M. Ho, A transferable tight-binding potential for carbon, J. Phys. 4 (28) (1992) 6047.
[39] G. Kresse, J. Hafner, Ab initio molecular-dynamics simulation of the liquid-metal–amorphous-semiconductor transition in germanium, Phys. Rev. B 49 (1994) 14251–14269.
[40] G. Kresse, J. Furthmüller, Efficient iterative schemes for ab initio total-energy calculations using a plane-wave basis set, Phys. Rev. B 54 (1996) 11169–11186.
[41] J.M. Soler, E. Artacho, J.D. Gale, A. Garca, J. Junquera, P. Ordejn, D. Snchez-Portal, The SIESTA method for ab initio order-n materials simulation, J. Phys. 14 (11) (2002) 2745.
[42] J.P. Mendez, F. Arca, J. Ramos, M. Ortiz, M.P. Ariza, Charge carrier transport across grain boundaries in graphene, Acta Mater. 154 (2018) 199–206.
[43] F. Arca, J.P. Mendez, M. Ortiz, M.P. Ariza, Steric interference in bilayer graphene with point dislocations, Nanomaterials 9 (7) (2019).
[44] J.H. Los, L.M. Ghiringhelli, E.J. Meijer, A. Fasolino, Improved long-range reactive bond-order potential for carbon. I. Construction, Phys. Rev. B 72 (2005) 214102.
[45] M.P. Ariza, M. Ortiz, Discrete crystal elasticity and discrete dislocations in crystals, Arch. Ration. Mech. Anal. 178 (2) (2005) 149–226.
[46] M.P. Ariza, M. Ortiz, Discrete dislocations in graphene, J. Mech. Phys. Solids 58 (5) (2010) 710–734.
[47] R.D. King-Smith, D. Vanderbilt, Theory of polarization of crystalline solids, Phys. Rev. B 47 (1993) 1651–1654.
[48] J. Perdew, K. Burke, M. Ernzerhof, Generalized gradient approximation made simple, Phys. Rev. Lett. 77 (1996) 3865–3868.
[49] J. Junquera, O. Paz, D. Sańchez-Portal, E. Artacho, Numerical atomic orbitals for linear-scaling calculations, Phys. Rev. B 64 (23) (2001).
[50] N. Troullier, J. Martins, Efficient pseudopotentials for plane-wave calculations, Phys. Rev. B 43 (1991) 1993–2006.
[51] A. Stukowski, Visualization and analysis of atomistic simulation data with OVITO-the open visualization tool, Modell. Simul. Mater. Sci. Eng. 18 (1) (2010).
[52] N.A. Spaldin, A beginner's guide to the modern theory of polarization, J. Solid State Chem. 195 (2012) 2–10.
[53] K.W. Lee, C. Lee, Strain-induced topological phase transition with inversion of the in-plane electric polarization in tiny-gap semiconductor SiGe monolayer, Sci. Rep. 10 (2020) 11300.
[54] S. Miyashita, Y. Konishi, M. Nishino, H. Tokoro, P.A. Rikvold, Realization of the mean-field universality class in spin-crossover materials, Phys. Rev. B 77 (2008) 014105.